



Article

Analysis of the Differences Between Two Landslides on One Slope in Yongguang Village Based on Physical Models and Groundwater Identification

Fucun Lu ¹, Kun Liu ^{1,2,3,*} , Shunhua Xu ^{1,2,3}, Jianyu Zhang ¹ and Dingnan Guo ¹ 

¹ Lanzhou Institute of Seismology, CEA, Lanzhou 730000, China; lufucun22@mailsucas.ac.cn (F.L.); 15735673486@163.com (D.G.)

² Key Laboratory of Loess Earthquake Engineering, Lanzhou Institute of Seismology, CEA, Lanzhou 730000, China

³ Gansu Earthquake Agency, Lanzhou 730000, China

* Correspondence: liukun@ggsdzj.gov.cn

Abstract: In 2013, a Ms 6.6 earthquake occurred at the boundary of Min County and Zhang County, triggering numerous landslides. Notably, two landslides with significantly different sliding characteristics emerged less than 100 m apart in Yongguang Village, Min County. The eastern landslide was characterized by instability induced by seismic inertial forces, whereas the western landslide exhibited flow slides triggered by liquefaction in loess. To further analyze the causes of these landslides, this study employed a 1 m depth ground temperature survey to probe the shallow groundwater in the area, aiming to understand the distribution of shallow groundwater. Based on the results from the 1 m depth ground temperature survey, a random forest model was applied to regressively predict the initial groundwater levels. The TRIGRS model was utilized to evaluate the influence of pre-earthquake rainfall conditions on landslide stability, and the pore water pressure outputs from TRIGRS were integrated with the Scoops3D model to analyze landslide stability under seismic effects. The results indicate that the combination of the 1 m depth ground temperature survey with high-density electrical methods and random forest approaches effectively captures the initial groundwater levels across the region. Notably, the heavy rainfall occurring one day prior to the earthquake did not significantly reduce the stability of the landslide in Yongguang Village. Instead, the abundant groundwater in the source area of the western landslide, combined with several months of pre-earthquake rainfall, resulted in elevated groundwater levels that created favorable conditions for its occurrence. While the primary triggering factor for both landslides in Yongguang Village was the earthquake, the distinct topographic and groundwater conditions led to significantly different sliding characteristics under seismic influence at the same slope.

Keywords: 1 m depth ground temperature survey; liquefaction-triggered flow slides in loess; TRIGRS; Scoops3D; random forest



Citation: Lu, F.; Liu, K.; Xu, S.; Zhang, J.; Guo, D. Analysis of the Differences Between Two Landslides on One Slope in Yongguang Village Based on Physical Models and Groundwater Identification. *Water* **2024**, *16*, 3591. <https://doi.org/10.3390/w16243591>

Academic Editor: Stefano Luigi Gariano

Received: 22 October 2024

Revised: 27 November 2024

Accepted: 6 December 2024

Published: 13 December 2024



Copyright: © 2024 by the authors. Licensee MDPI, Basel, Switzerland. This article is an open access article distributed under the terms and conditions of the Creative Commons Attribution (CC BY) license (<https://creativecommons.org/licenses/by/4.0/>).

1. Introduction

Earthquakes often lead to numerous direct and secondary disasters, among which soil liquefaction is a highly destructive seismic hazard closely related to groundwater movement [1]. Liquefaction-induced landslides occur when saturated loess on slopes experiences significant increases in pore water pressure due to strong seismic shaking, resulting in reduced effective stress and subsequent liquefaction. This process creates a sliding surface (or zone) within the liquefied soil layer, causing the overlying unsaturated soil to slide or resulting in mudflow. The sliding surfaces in these types of landslides typically consist of the liquefied soil layer or a momentarily formed water film between the liquefied soil and an overlying impermeable layer. Such landslides can have long sliding distances, often spanning several square kilometers, with lengths ranging from one to

several kilometers, posing severe threats to the safety of residents in mountainous areas and to major engineering projects [2].

Although large-scale soil flow resulting from the liquefaction of deep saturated soil layers triggered by earthquakes is a rare disaster, several significant historical earthquakes have indeed caused such events. For instance, the Ms 8.5 Haiyuan earthquake in 1920 triggered liquefaction-induced landslides in the Shibei Yuan area of Guyuan City and the Dangjiacou landslide in Ningxia [3–5]. A recent example of liquefaction-triggered flow slides in loess occurred on 18 December 2023, during a 6.2 magnitude earthquake in Jishihang County, Gansu Province, which triggered a typical seismic liquefaction-triggered flow slide in loess in Jintian and Caotan villages in Minhe County, Qinghai Province. A similar loess liquefaction mudflow disaster occurred in Yongguang Village, triggered by the Ms 6.6 earthquake in Minxian and Zhangxian on 22 July 2013. Both disasters shared similar external triggering factors; first, Zhongchuan Township had been engaged in long-term irrigation and a three-day winter irrigation was conducted just before the earthquake. On the other hand, Yongguang Village was in the rainy season prior to the earthquake. According to data from the Minxian Meteorological Station, the rainfall in July 2013 was twice the historical average for July. The winter irrigation in Zhongchuan Township and the unusual rainfall in Yongguang Village were both significant external factors contributing to the loess liquefaction mudflow [6]. However, in Yongguang Village, two highly destructive landslides with markedly different flow and sliding characteristics occurred on the same slope. The western landslide manifested as a loess liquefaction mudflow, while the eastern landslide was triggered by seismic inertial forces. It is speculated that groundwater may play a key role in controlling this difference. Research by Chen Longwei et al. [7] indicates that future studies should focus on investigating the correlation between regional hydrogeological conditions and disasters and whether liquefaction-induced landslides are isolated incidents or have broader implications. Therefore, understanding the distribution and storage of shallow groundwater is crucial for the prevention and control of geological disasters in landslide-prone areas.

Numerous scholars have conducted extensive research on the Yongguang Village landslides. Xu Shunhua et al. analyzed the spatial distribution characteristics, occurrence, development processes, and triggering mechanisms of the landslides based on field investigations, precipitation data, and aerial imagery [8]. Wu Zhijian et al. conducted field surveys, borehole sampling, and high-density surface wave exploration at the western landslide of Yongguang Village, revealing the topographic conditions and soil layer distribution. They also employed dynamic finite element methods and strength reduction techniques to analyze the mechanisms underlying the western landslide [9]. Wang et al. determined the loess characteristics of the western landslide in Yongguang Village through field investigations and laboratory triaxial tests, evaluating the site response to seismic motion, slope stability, and liquefaction potential [10]. Wang Lanmin et al. constructed a test model based on the saturated liquefaction mudflow in Yongguang Village and conducted shaking table experiments to validate the disaster mechanisms associated with saturated liquefaction-induced mudflow on loess slopes [2]. Previous research indicates that the liquefaction-triggered flow slides in loess in Yongguang Village are related to abnormal rainfall prior to the earthquake and that groundwater is a critical geological parameter in landslides [11]. However, few scholars have investigated the distribution and storage of shallow groundwater in the area, nor have they analyzed the reasons for the significantly different sliding characteristics of the two landslides. The shallow temperature measurement method can be used to infer the location, flow path, and scale of groundwater, offering advantages such as cost-effectiveness, environmental friendliness, speed, and simplicity [12]. This method aids in identifying potential landslide areas, as the analysis of temperature distribution can provide valuable information about shallow groundwater flow.

Numerous scholars have conducted in-depth studies on the use of temperature methods for shallow groundwater investigations. Kappelmeyer et al. implemented 1.5 m temperature observations to investigate how gradually rising groundwater affects shallow

temperature distribution [13]. Furuya conducted temperature measurements at a depth of 1 m in areas susceptible to landslides, elucidating the relationship between the distribution of actual slope failures and groundwater systems [14]. Chen Xiaodong further explored the feasibility of using shallow temperature measurement methods for investigating flowing groundwater and conducted numerical simulations and quantitative analyses [12]. Furuya et al. installed thermocouples at a depth of 1 m in the main body of the Nishikawa landslide in Tokushima, Japan, successfully estimating the position of groundwater flow through continuous monitoring [15]. Yasuda et al. effectively detected the distribution of groundwater flow in Hokkaido using the 1 m depth ground temperature survey and established mitigation measures, such as drilling and well installation, based on the measurements, successfully halting a landslide that had been moving 20 cm per month [16]. Thus, the 1 m depth ground temperature survey proves to be an effective method for investigating groundwater flow. However, landslides are natural disasters triggered by multiple factors and their occurrence is complex, meaning that landslide susceptibility cannot be evaluated based solely on groundwater. Rainfall-induced landslide prediction methods based on physical models simulate the landslide process by incorporating geomorphological and geomechanical features, making them effective tools for shallow landslide susceptibility analysis. This approach can replicate the physical processes of landslides, providing a scientific foundation for landslide risk assessment.

Currently, one of the most significant physical models for predicting rainfall-infiltration-induced slope instability is TRIGRS, which accounts for the effects of transient pore water pressure. This model can predict the impact of short-duration, intense rainfall on groundwater changes and output the spatial distribution of pore water pressure to the Scoops3D model. The Scoops3D model incorporates a horizontal seismic acceleration coefficient to assess slope stability under seismic conditions. Salciarini et al. conducted susceptibility assessments of shallow landslides in the Seattle area of Washington State using the TRIGRS model, calculating the predicted landslide probability distribution for various recurrence intervals [17]. Reid et al. successfully predicted the stability of landslides in volcanic ash layers in coastal areas using Scoops3D [18]. Tran et al. integrated the three-dimensional slope stability model Scoops3D, developed by the USGS, with the TRIGRS model to create a 3D rainfall spatial-temporal landslide prediction assessment model. The results demonstrated that this model is highly effective for evaluating rainfall-induced landslide predictions in specific areas [19]. Yang Liu et al. combined the TRIGRS model with a random forest model to select suitable non-landslide samples, assessing landslide susceptibility in the Yongjia region of Zhejiang Province due to typhoon impacts [20]. While the TRIGRS model effectively enhances the accuracy of spatiotemporal landslide predictions by calculating the impact of varying rainfall amounts on slope stability in real time, it is highly sensitive to the input parameters required, such as soil hydraulic conductivity, initial groundwater levels, and soil depth. Accurately obtaining these parameters can be challenging [21,22]. Wu et al. [23] used high-density electrical method inversion data combined with borehole data to accurately estimate the approximate location of the groundwater table in the loess plateau area. However, this method struggles to provide the spatial distribution of the initial groundwater table required by the TRIGRS model.

Therefore, we utilized high-density electrical resistivity data and borehole data, in conjunction with results from the 1 m depth ground temperature survey, to employ a random forest model for regressive prediction of the initial groundwater levels in Yongguang Village. This approach allowed us to obtain the spatial distribution of the initial groundwater level. Additionally, through field investigations, we applied the co-kriging method to obtain relatively accurate soil layer thickness measurements. The TRIGRS model was used to assess the impact of slope stability under conditions of no rainfall, actual rainfall, and intense rainfall, producing corresponding pore water pressure results. Based on this, the Scoops3D model was employed to evaluate the combined effects of earthquakes, groundwater, and rainfall on landslide stability in the study area. Additionally, the analysis focused on the causes of liquefaction-triggered flow slides in the loess of Yongguang Village.

2. Study Area

Min County is located at the northeastern edge of the Tibetan Plateau, serving as a transitional zone between the Gannan Plateau, the Longxi Loess Plateau, and the Longnan Mountains. The region has a complex geological structure and undulating terrain [24]. Yongguang Village, located in the northern part of Min County, lies on the northeastern edge of the Tibetan Plateau and is influenced by multiple major active faults, resulting in significant tectonic activity. The surface trace of the Hetuo Fault crosses through Yongguang Village (Figure 1), causing surface fragmentation and severe soil erosion in the area.

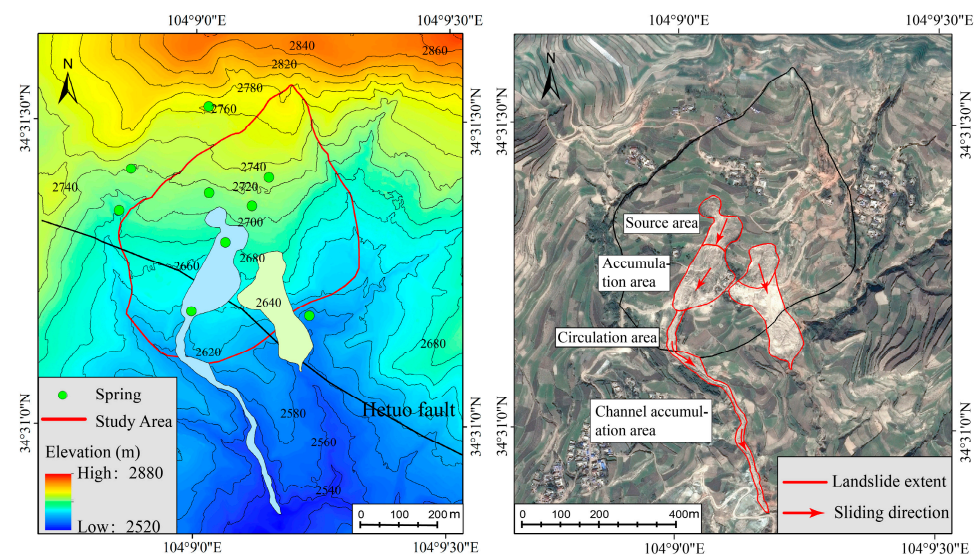


Figure 1. Topographic and Google Earth imagery of Yongguang Village.

Yongguang Village is situated on a south-facing slope with an average gradient of 17.2° , characteristic of a typical loess–red clay composite slope. The stratigraphic structure of the slope is relatively simple, primarily consisting of aeolian Q_3 loess, with unevenly distributed silty soil and surface cultivated soil. The lithology of the slope can be classified into two categories: (1) Neogene (N), composed of siltstone and mudstone; (2) Upper Pleistocene (Q), predominantly consisting of loess and silt. Large gullies on both the east and west sides form a relatively independent and enclosed small watershed, leading to complex hydrological conditions. The groundwater types include pore water from Quaternary aquifers and fissure water from Neogene sandstones [25]. The Neogene mudstone (red clay) acts as a relatively impermeable layer, with groundwater distributed in a vein-like manner and being relatively abundant.

Loess is a fragmented, porous, multi-phase granular material with a loose structure and well-developed pores. When exposed to water or subjected to moderate to strong seismic forces, its structure can undergo catastrophic collapse, leading to a sudden and complete loss of strength [26]. Red clay, on the other hand, is an over-consolidated, hard, cohesive soil with poor permeability and, together with the overlying loess, it forms a typical loess–laterite composite slope. At the interface between loess and laterite, high-saturation moisture accumulation zones often form, which softens the soil and reduces its strength [27]. The combined characteristics of these two soil types contribute to the frequent occurrence of loess landslides in the area, causing significant damage.

3. Methods

To comprehensively analyze the formation causes of two landslides with significantly different flow characteristics on the same slope in Yongguang Village, this study employed the 1 m temperature method to investigate the distribution of shallow groundwater in the research area. Based on the results of the 1 m temperature method, a regression prediction

of the initial groundwater levels was conducted using a combination of random forest modeling and high-density electrical method results. After obtaining accurate hydrological and geotechnical parameters, the TRIGRS model was utilized to assess the impact of actual rainfall on landslide stability. Furthermore, by considering the pore water pressure induced by actual rainfall and groundwater, the Scoops3D model was applied to analyze the stability of the landslides in the study area under seismic influence. The final analysis revealed that, although both landslides occurred on the same slope, the western landslide exhibited flow slides induced by seismic liquefaction, while the eastern landslide demonstrated instability triggered by seismic inertial forces, highlighting the specific influencing factors involved. Figure 2 provides an overview of the research workflow.

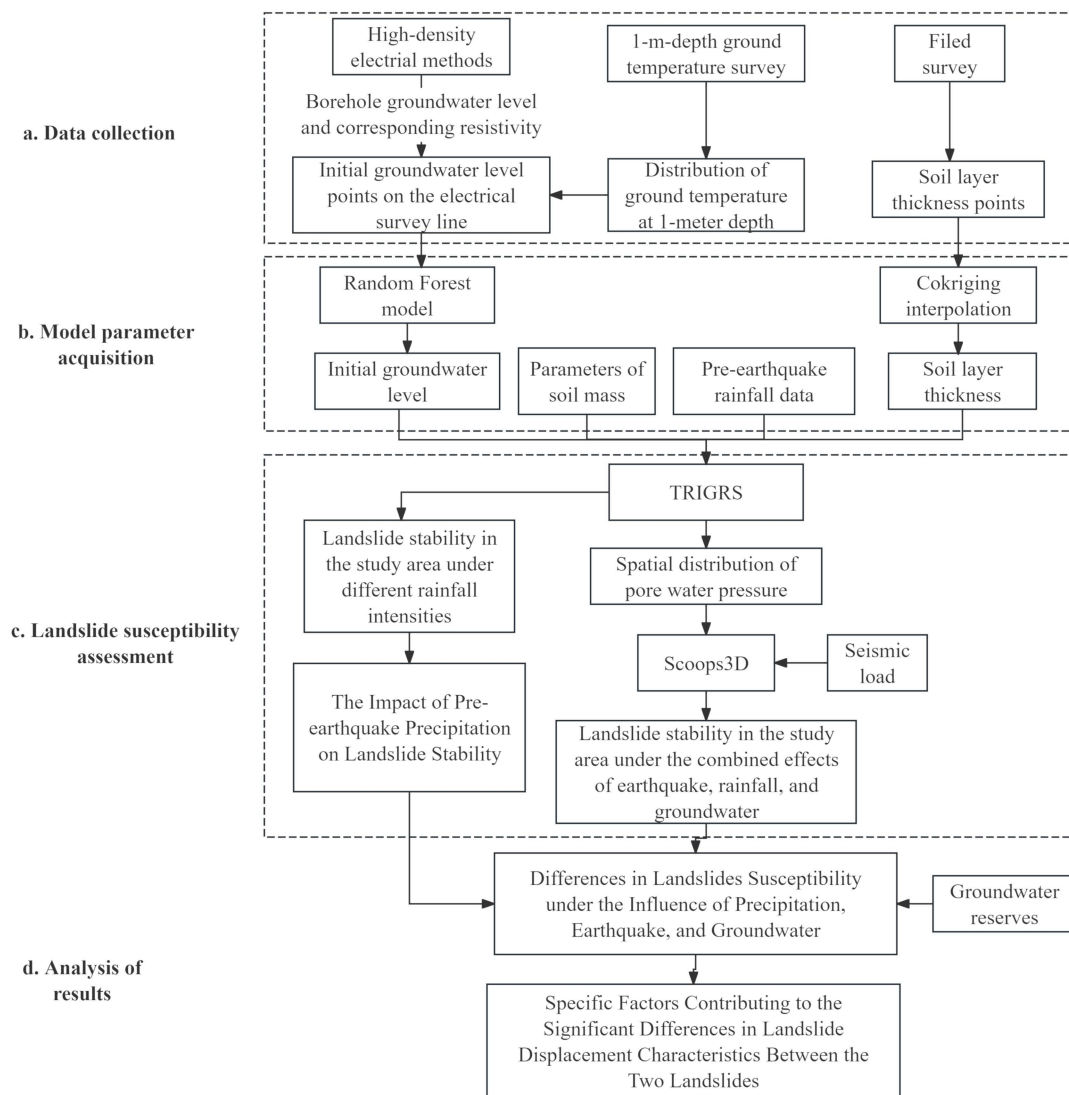


Figure 2. Flowchart showing the methodology of this study.

3.1. One-Meter-Depth Ground Temperature Survey

3.1.1. Principle of the 1 m Depth Ground Temperature Survey

The movement of groundwater involves heat exchange with surrounding materials, resulting in alterations to the regional ground temperature conditions. Thus, the movement of regional groundwater plays a crucial role in controlling ground temperature distribution. When the scale of a groundwater system at a certain burial depth is sufficiently large, it can influence the temperature field of shallow strata, leading to anomalies in the normal

ground temperature field. Detecting these anomalies with temperature sensors allows for the identification of relevant information about flowing groundwater systems, which constitutes the fundamental principle of using shallow ground temperature measurements to investigate flowing groundwater [12]. Takeuchi was one of the first to use shallow soil temperature measurement methods to study groundwater in landslide-affected areas [28]. Furuya et al. estimated the location of groundwater flow paths within the landslide mass by analyzing 1 m soil temperature variations [15]. Yasuda et al. conducted a 1 m soil temperature survey to investigate groundwater in landslide areas and implemented landslide mitigation measures through groundwater drainage [16].

Due to the influence of shallow groundwater systems, ground temperatures near these systems are often lower than the average temperatures from summer to autumn. Conversely, ground temperatures adjacent to groundwater are typically higher during winter to spring. When the temperature difference between the normal ground temperature and the flowing groundwater temperature at a depth of 1 m exceeds 2.5 °C, a 1 m ground temperature survey can be conducted [15]. The optimal periods for conducting such surveys are typically from July to November and from January to April, as shallow ground temperatures during these times are significantly influenced by air temperatures, leading to a greater temperature differential with water, which can yield more accurate results [10].

3.1.2. Measurement Process of the 1 m Depth Ground Temperature Survey

Instrumentation: Ground drilling machine, split-type temperature sensor, GPS.

The measurement schematic is illustrated in Figure 3, with data collection conducted from 7 July to 5 August. The split-type temperature sensor used (accuracy: 0.01 °C) is a 1.2 m long stainless steel rod with the sensor located at its tip. The tip is inserted into the ground to a depth of one meter, and the reading is taken by connecting it to a separate display unit. For relatively hard ground surfaces, a 1 m deep hole is first drilled at the intended measurement location using the ground drilling machine, after which the temperature sensor is placed into the hole and buried. Measurements are recorded after waiting 10 min for the readings to stabilize, along with GPS location data. For softer soils, the drilling step can be skipped and the sensor can be directly inserted to a depth of 1 m, with the remaining steps identical to those of the drilling method.

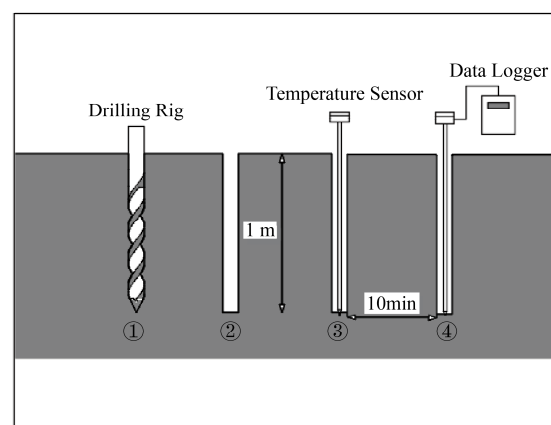


Figure 3. Schematic diagram of 1 m depth ground temperature survey.

3.2. Random Forest

Random forest is an ensemble learning model that belongs to the bagging category. Breiman introduced it in 2001 by combining classification tree algorithms [29]. RF uses classification and regression tree (CART) decision trees as weak classifiers and builds a more effective ensemble algorithm by combining a large number of decision trees. The model construction process introduces two types of randomness: sample randomness and feature randomness. Ultimately, the model's results have high accuracy and generalization

performance, achieved through voting or averaging [30]. By randomly selecting samples and features, the random forest model mitigates the risk of overfitting to some extent and effectively evaluates the contribution of each feature to the predictive outcomes.

3.3. TRIGRS

The TRIGRS model is a grid-based slope stability calculation model developed by the U.S. Geological Survey, designed to compute changes in pore water pressure due to rainfall infiltration and the corresponding safety factor. It consists of three modules: infiltration, hydrology, and slope stability.

The rainfall infiltration module is based on the linear solution of Richards' equation proposed by Iverson [31], which calculates the seepage conditions at specified depths within soil layers over a given time period, accurately reflecting seepage changes under rainfall infiltration conditions. The hydrology module assumes water conservation within each computational grid cell during each time interval, meaning that any rainfall that cannot infiltrate will flow as surface runoff to downstream grids, thus preventing any arbitrary loss of water.

The TRIGRS model is based on the infinite slope model analysis and is applicable to landslides occurring at relatively shallow depths. When considering variations in groundwater pore water pressure, the model can determine the stability of grid cell units at different depths, where the safety factor (F_s) is defined as the ratio of anti-sliding force to sliding force [32,33]. The expression is as follows:

$$F_s(Z, t) = \frac{\tan \varphi}{\tan \delta} + \frac{c - \psi(Z, t)\gamma_w \tan \varphi}{\gamma_s Z \sin \delta \cos \delta} \quad (1)$$

where c is the effective cohesion of the soil, φ is the effective internal friction angle of the soil, γ_w is the unit weight of water, γ_s is the natural unit weight of the soil, $\psi(Z, t)$ is the pressure head in the unsaturated layer, and F_s is the factor of safety.

3.4. Scoops3D Model

The Scoops3D model, developed by the U.S. Geological Survey (USGS), is based on digital elevation models and calculates the grid safety factors on various sliding surfaces using a three-dimensional simplified Bishop's method [18]. The model defines sliding surfaces through a circular arc search method, where several search points are established based on defined parameters. For each search point, spheres with incrementally increasing radii are drawn, and the intersections of these spheres with the digital elevation model define the sliding surfaces.

Scoops3D computes a factor of safety, F , for a given trial surface using moment equilibrium. The safety factor can be expressed as the ratio of average shear resistance (strength), S , to the shear stress, τ . A higher safety factor indicates greater stability of the sliding block. The calculation of the safety factor is as follows:

$$F_S = \frac{S}{\tau} \quad (2)$$

The shear strength of the soil s is calculated using the Mohr–Coulomb criterion:

$$s = c + (\sigma_n - u) \tan \phi \quad (3)$$

In the equation, c represents soil cohesion, ϕ is the internal friction angle of the soil, σ_n is the normal stress acting on the sliding body, and u is the pore water pressure on the shear plane.

The Scoops3D stability model incorporates seismic loads by defining a horizontal seismic acceleration coefficient (K_{eq}), which is considered a horizontal force acting on the sliding mass. Based on the moment equilibrium of forces acting on the sliding body within the grid cell (Figure 4), the sum of gravitational forces W , seismic loads WK_{eq} ,

and tangential forces s must equal zero at the center of the sphere. Here, e represents the vertical distance from the sphere center to the center of mass of the sliding body, while other parameters are indicated in the illustration.

$$\tau_{i,j}A_{i,j}R_{i,j} - W_{i,j}R_{i,j} \sin \alpha_{i,j} - W_{i,j}K_{eq}e_{i,j} = 0 \tag{4}$$

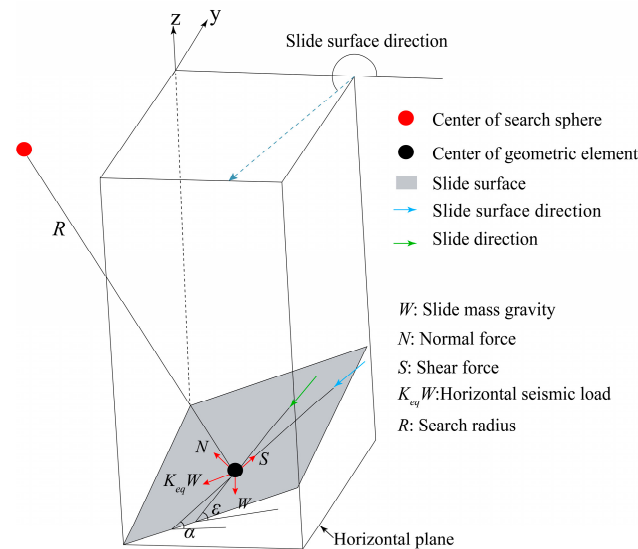


Figure 4. Schematic diagram of cell grid (cited from Li et al. [34]).

Based on the vertical force balance, the sum of the gravitational force W , the vertical component of the normal force $N = \sigma_n A$, and the vertical component of the tangential force S equals zero:

$$\sigma_{i,j}A_{i,j} \cos \varepsilon_{i,j} + \tau_{i,j}A_{i,j} \sin \alpha_{i,j} - W_{i,j} = 0 \tag{5}$$

By solving for shear stress τ and normal stress σ_n using Equations (4) and (5) and substituting them into Equations (3) and (2), the three-dimensional stability coefficient formula can be obtained (in the equation, $m_{a_{i,j}} = \cos \varepsilon_{i,j} + \sin \alpha_{i,j} \tan \phi_{i,j} / F_s$):

$$F_s = \frac{\sum R_{i,j}[c_{i,j}A_{i,j} \cos \varepsilon_{i,j} + (W_{i,j} - u_{i,j}A_{i,j} \cos \varepsilon_{i,j}) \tan \phi_{i,j}]/m_{a_{i,j}}}{\sum W_{i,j}[R_{i,j} \sin \alpha_{i,j} + K_{eq}e_{i,j}]} \tag{6}$$

4. Results

4.1. Results of 1 m Depth Ground Temperature Survey

Field measurements for 1 m ground temperature were conducted at intervals of 5 to 10 m along the east–west direction. Due to topographical influences, the spacing for north–south measurements varied from 10 to 40 m, with an average of 25 m. A total of 733 temperature measurement points were recorded, as illustrated in Figure 5a. Based on previous geological disaster occurrences, field investigations, and the terrain of the study area, it was determined that the central-southern and eastern regions are high-risk areas for geological disasters, while the northern region remains relatively stable. The eastern terrain is particularly complex, making it challenging to measure according to the predetermined density. Consequently, during point collection, measurements in the central-southern region were denser, while those in the northern and eastern regions were comparatively sparse.

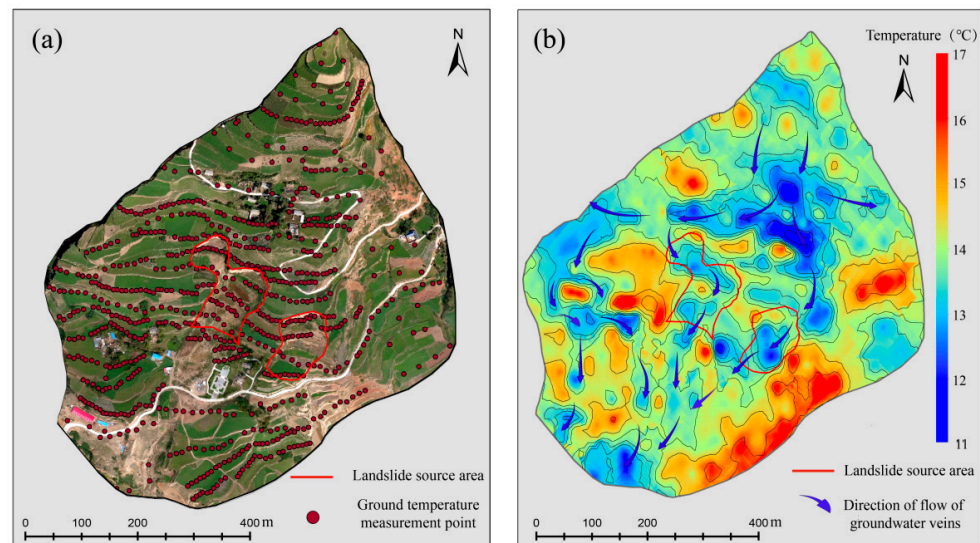


Figure 5. Results of 1 m depth ground temperature survey: (a) distribution of temperature measurement points; (b) distribution of 1 m ground temperature and inferred direction of groundwater flow vein in Yongguang Village.

The average temperature recorded across all measurement points was 14.28 °C, with a maximum temperature difference of 6.48 °C, which is significantly greater than 2.5 °C. This indicates that the study area is suitable for conducting investigations into 1 m depth ground temperature survey. Since the 1 m ground temperature data obtained from field measurements were distributed as point data, this study employed interpolation methods to derive a continuous surface distribution of ground temperature across the research area. The interpolation process included the following steps: data input, data preprocessing, experimental variogram calculation, variogram fitting, kriging interpolation, and contour mapping. The final interpolation results are illustrated in Figure 5b.

The topography of Yongguang Village is characterized by higher elevations in the north and east and lower elevations in the south and west, with significant gully formations on both the east and west sides, resulting in a vertical difference of up to 180 m. This substantial elevation variation provides a constant driving force for shallow groundwater. According to the principles of shallow temperature measurement, the lines connecting the extrema of the temperature field indicate the flow paths of shallow groundwater [35]. Based on the terrain of the study area and the locations of spring outlets, the overall direction of shallow groundwater flow is from the northern region towards the southwest, which aligns with the general topographical gradient of higher elevations in the north and east and lower elevations in the south and west.

4.2. Initial Groundwater Level Depth

Accurate initial groundwater level information is essential for enhancing the temporal and spatial prediction accuracy of landslides. In this study, we performed a comparative analysis by integrating high-density electrical resistivity inversion data [25] with measured groundwater levels from drilling b and e, which are closest to the survey lines (Figure 6). Based on these data, we inferred that the resistivity near the groundwater levels in the study area ranges from 30 to 40 Ω·m. Using these findings, we extracted 51 initial groundwater depth points as sample data and employed the random forest model to predict the initial groundwater depth distribution across the study area (Figure 7).

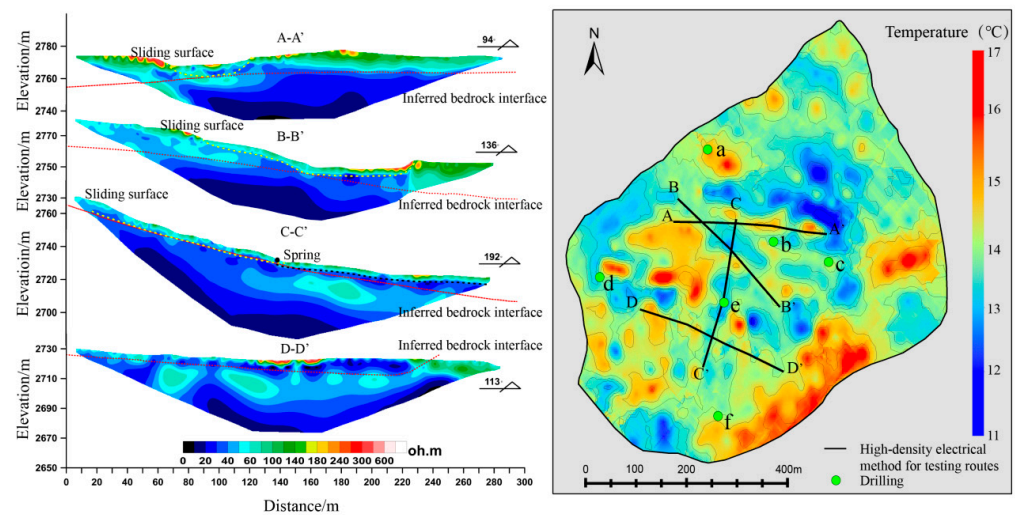


Figure 6. Results of the high-density electrical method and distribution of measurement lines.

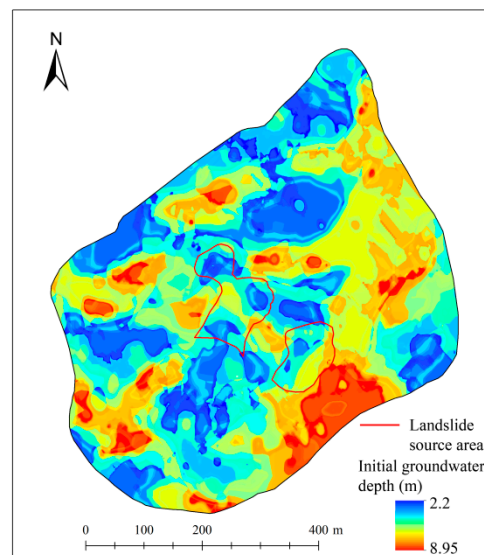


Figure 7. Initial groundwater level in the study area.

The study area is characterized by typical loess topography, where the shallow groundwater system is primarily recharged by precipitation. After rainfall events, flatter regions serve as more favorable runoff accumulation zones, facilitating greater infiltration and replenishing the groundwater. Additionally, the depth of the groundwater significantly affects the soil temperature at a 1 m depth. Therefore, soil temperature at 1 m depth and slope were selected as training variables for the random forest model, which was then used to predict the initial groundwater depth.

To address potential issues related to insufficient training and validation data, we utilized the Jackknife method in the reliability analysis of the random forest model. Specifically, 90% of the sample points were used as training data, while the remaining 10% served as validation data. This process was repeated 51 times to obtain predictions for all sample points. Ultimately, the coefficient of determination (R^2) for the fit between the predicted values derived from the random forest model and the actual values was 0.93 (Figure 8), where the blue dots represent the predicted and actual values for the points used for model validation in each iteration.

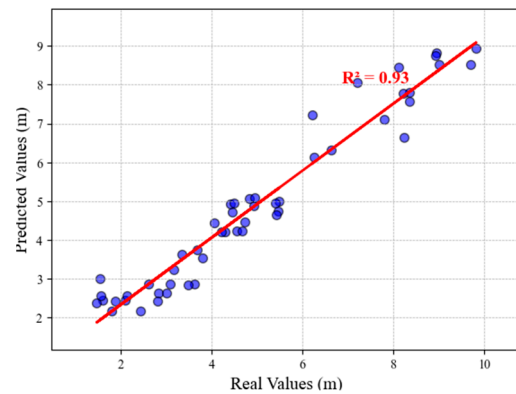


Figure 8. Prediction accuracy of the random forest (RF) model.

4.3. Soil Layer Thickness

In the TRIGRS model, soil thickness represents the deepest potential failure surface, which is typically the surface with the lowest safety factor. For this study, the soil layer thickness is defined as the distance from the surface to the underlying red clay. Due to intense erosion, fragmented topography, frequent geological disasters, and terracing activities in the study area, numerous red clay exposures were identified. Through field investigations, we obtained 19 soil thickness measurement points, along with 4 borehole data, totaling 23 points of soil thickness. The investigation revealed that the erosion conditions in the study area intensify from west to east, influenced by slope, precipitation, and ancient landslides. Referring to the geomorphological index soil thickness model (GIST) proposed by Catani [36], we selected two auxiliary variables (Figure 9a): the north–south slope position (P_1) and the east–west relative position (P_2) for co-operative kriging interpolation. This approach yielded a distribution map of soil layer thickness across the study area (Figure 9b). The average standard error of cross-validation was 1.79 m. Although this error is relatively high, it remains acceptable given that the range of actual values spans 22 m.

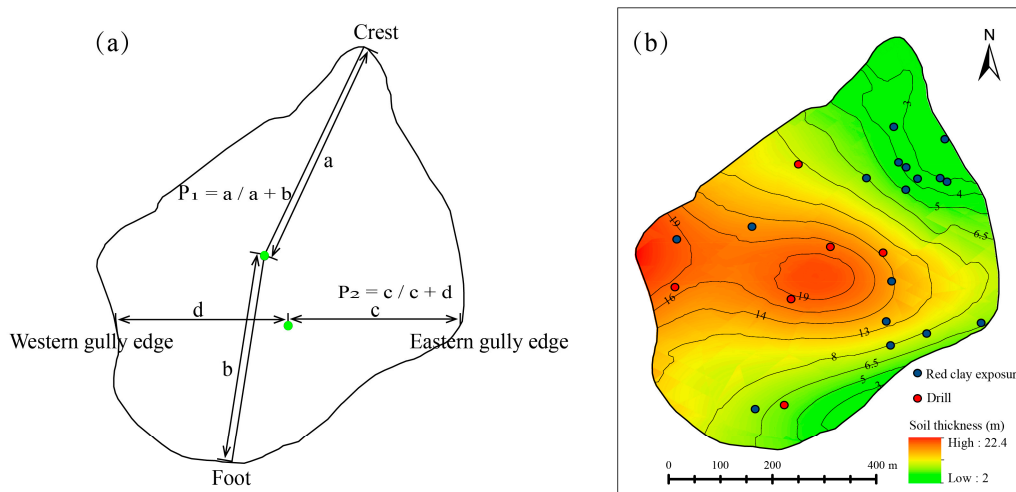


Figure 9. Illustration of the auxiliary variable used in co-kriging interpolation of soil layer thickness and the resulting interpolation outcomes: (a) schematic diagram illustrating the relative position P_1 , P_2 at a point on the slope surface; (b) soil thickness in the study area.

4.4. Soil and Water Parameters

Soil and water parameters primarily include the angle of internal friction, soil cohesion, initial groundwater depth, vertical hydraulic conductivity of saturated soil, hydraulic diffusivity, and unit weight of soil. The specific parameter values are provided in Table 1. The soil cohesion and internal friction angle data used in this study were sourced from the Lanzhou Institute of Seismology [10].

Undisturbed loess samples with an approximate volume of $200 \times 200 \times 300$ mm were taken from a scarp by manual excavation behind the head of the landslide. To ensure that the samples maintained their original stress state, approximately 1 m of material was excavated from the steep slope surface prior to sampling. Samples were collected from a depth of 8.0 to 8.3 m below the surface. Key parameters, including soil cohesion and internal friction angle, were obtained through a series of dynamic triaxial tests. Relevant studies indicate that the unit weight of soil in the study area is 17.1 kN/m^3 [37], while the saturated hydraulic conductivity is $5 \times 10^{-6} \text{ m/s}$ [38]. Additionally, the hydraulic diffusivity of the soil is 100 times the saturated hydraulic conductivity, measuring $5 \times 10^{-4} \text{ m}^2/\text{s}$.

Table 1. Parameters of soil mass.

Soil Mass	Cohesion (kPa)	Internal Friction Angle ($^\circ$)	Unit Weight of Soil (kN/m^3)	Vertical Hydraulic Conductivity of Saturated Soil (m^2/s)	Hydraulic Diffusivity (m^2/s)
	50.74	16.52	17.1	5×10^{-4}	5×10^{-6}

4.5. Results of the TRIGRS Model

This study employed a TRIGRS model to assess the factor of safety (FS) values for each grid cell in the research area under three scenarios (Figure 10): no rainfall, actual rainfall, and heavy rainfall (100 mm/day). The analysis was based on a 10 m resolution digital elevation model (DEM) and precise soil and water parameters. The actual rainfall parameters were set according to data from the nearest automated weather station to Yongguang Village, with an initial rainfall of 3 mm/h for the first 3 h, followed by 1 mm/h for the subsequent 9 h [25]. The FS values were categorized into four levels: high-susceptibility areas, medium-susceptibility areas, low-susceptibility areas, and stable areas. Specifically, when FS is less than 1, the grid is considered extremely unstable and classified as a high-susceptibility area; when FS is greater than 1 but less than 1.2, it is categorized as a moderate-susceptibility area; FS values between 1.2 and 1.5 indicate a low-susceptibility area; and values greater than 1.5 denote a stable condition.

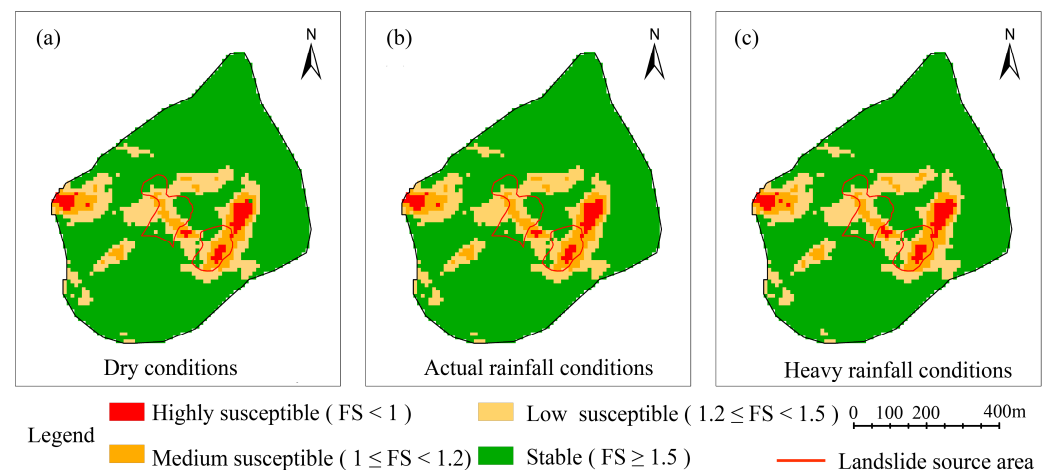


Figure 10. Results of the TRIGRS model: (a) dry conditions, (b) actual rainfall conditions, and (c) heavy rainfall conditions.

The results of the TRIGRS model indicate that, in the absence of rainfall, both the eastern and western landslide source areas contain small zones of medium susceptibility. Rainfall-induced landslide susceptibility is primarily concentrated in the eastern and western parts of the study area. Statistically, under dry conditions, high-susceptibility zones

account for 2% of the total area, medium-susceptibility zones for 5.4%, low-susceptibility zones for 15.5%, and stable zones for 77.1%. Under actual rainfall conditions, the landslide susceptibility across the study area shows little variation. During heavy rainfall events, the area classified as high susceptibility increases by only 0.2% compared to dry conditions, while moderate susceptibility increases by 0.4% and low susceptibility by 0.1%. Thus, sudden intense rainfall does not appear to be the dominant factor triggering landslides in the study area. However, water infiltration increases the bulk density of the soil, softens the soil, and reduces its shear strength, thereby promoting slope deformation.

4.6. Results of the Scoops3D

The M_s 6.6 earthquake in Min County was characterized by an epicenter intensity of VIII. The Yongguang landslide is situated within this intensity zone, where intensity VIII corresponds to an equivalent peak ground acceleration range of 0.18 to 0.36 g [10]. Therefore, a peak ground acceleration coefficient of 0.2 was chosen. Utilizing a pre-earthquake digital elevation model (DEM) with a resolution of 10 m, the TRIGRS model was applied to determine pore water pressure inputs for the Scoops3D model under two scenarios: one without groundwater and the other with actual rainfall conditions. This approach allows for the assessment of landslide stability in the study area under both circumstances (Figure 11).

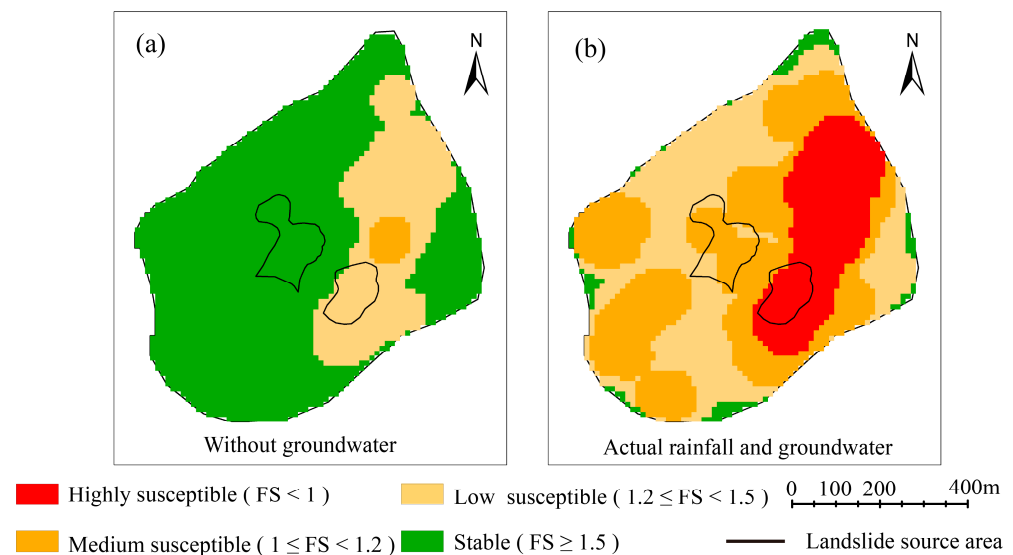


Figure 11. Results of the Scoops3D model: (a) conditions without groundwater; (b) conditions with actual rainfall and groundwater.

The results from Scoops3d indicate that, under a peak ground acceleration coefficient of 0.2 g, the eastern part of the study area exhibits some medium susceptible zones, though it remains generally stable. However, under the combined effects of rainfall, groundwater, and seismic activity, the factor of safety (FS) in the study area significantly decreases. Statistical analysis reveals that the average FS for western landslides dropped from 1.42 to 1.20, while, for eastern landslides, it declined from 1.13 to 0.93. Overall, the eastern landslide region is in an unstable state, while the western landslides, despite a considerable decrease in average FS, continue to exhibit relative stability state. Lu Li's research [39] indicates that the peak ground acceleration (PGA) of seismic motion from the Min-Zhang earthquake significantly increased at the surface layer when the overburden exceeded 20 m, showing a clear inflection point. At the same elevation, the PGA could vary by 1 to 2 times. Figure 9b illustrates that the two landslide source areas in Yongguang Village have the thickest soil layers in the study region. Therefore, the amplification effect of seismic motion due to topographical conditions is also a reason for the overestimation of the Fs values in the model.

The TRIGRS model combined with the Scoops3D model provides good predictive capabilities for rainfall-induced landslides triggered by earthquakes; however, it performs poorly for predicting flow slides caused by loess liquefaction, a specific type of geological hazard, and is limited in accounting for the topographical amplification effect. Loess liquefaction flow slides are closely related to groundwater interactions. For such specific types of landslides, greater attention should be paid to their unique hydrogeological conditions.

5. Discussion

The results from the TRIGRS model indicate that sudden rainfall does not significantly reduce the landslide stability in the study area. In contrast, the findings from the Scoops3D model reveal that the stability of the eastern landslide in Yongguang Village experiences a substantial decline under seismic activity, with the overall factor of safety (FS) dropping below 1, averaging 0.93. While the FS for the western landslide also decreases significantly due to seismic effects, it remains relatively high, with an average FS of 1.2, indicating a stable condition. However, liquefaction-triggered flow slides in loess occurred in this area under seismic influence, despite the relatively flat terrain prior to the earthquake, which led to more destructive disasters. This suggests that groundwater plays a crucial role in controlling the occurrence of such disasters.

5.1. Landslide Mechanism Analysis

The study area is located in the Longzhong region, where Neogene red clay is widely distributed. The poor cementation of the red clay, combined with a significant cover of loess, results in a typical loess slope primarily composed of loess and red clay. Factors such as topographic gradient and surface lithology influence the weak groundwater recharge in the loess hilly area. The presence of red clay acts as a barrier, causing moisture entering the slope to accumulate at the lithological interface, leading to the formation of a highly saturated soil layer. Therefore, by assuming that the groundwater table is rich in water up to the upper boundary of the red clay layer, the groundwater storage capacity can be calculated by subtracting the depth of the groundwater from the distance between the red layer interface and the surface (Figure 12).

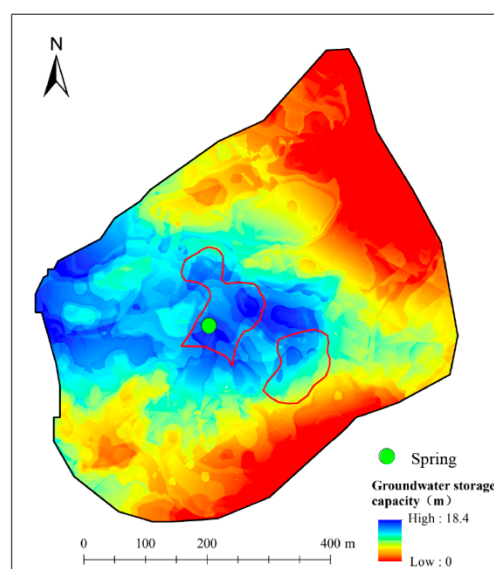


Figure 12. Groundwater storage capacity.

Figure 12 demonstrates that the groundwater reserves in the area of the western landslide are the most abundant in the entire study region, whereas the eastern landslide is located in an area with relatively low groundwater reserves. Prior to the earthquake, a spring existed in the source area of the western landslide, which local residents relied on for

drinking water, further confirming the substantial groundwater availability in this region. Terrain analysis reveals that the slope west of Yongguang Village exhibited a topographical trend characterized by low elevation in the center and higher elevations on either side prior to the earthquake. Following rainfall, a significant amount of rainwater accumulates in the landslide area, leading to substantial infiltration and groundwater recharge. In contrast, the original topography of the eastern landslide is higher in the center and lower on the sides, causing most of the rainwater to flow away along the slope rather than infiltrate. As a result, the western landslide area possesses a larger surface runoff area and is more influenced by regional topography, facilitating greater rainwater recharge. The topographical characteristics of the western landslide determine its enhanced capacity for groundwater replenishment, while the eastern landslide has relatively low groundwater reserves and minimal rainwater infiltration.

According to data from the Min County Meteorological Station, the average annual rainfall in the region from 1960 to 2019 was 596.5 mm. In 2013, total rainfall reached 709.9 mm, with a historical average of 104.3 mm for July; however, in July 2013, rainfall was recorded at 204.2 mm, nearly double the historical average for that month [10]. The abundant groundwater in the landslide source area of the westward landslide, coupled with several months of rainfall prior to the earthquake, caused the groundwater table to rise, making the sliding mass more saturated, increasing the weight of the soil, and softening the sliding zone [40], thereby providing favorable conditions for the occurrence of loess liquefaction mudflows. Consequently, after the earthquake, the eastward landslide was triggered by seismic inertial forces, while the westward landslide, with its rich groundwater reserves and rainwater recharge leading to further groundwater elevation, experienced loess liquefaction mudflows due to structural damage to the loess, volumetric contraction, and a sustained increase in pore water pressure.

5.2. Analysis of Landslide-Prone Areas in the Study Region

Overlaying the areas with a factor of safety (FS) value less than 1 (red zone), as outputted by the Scoops3D model, with terrain shadow maps and historical landslide data revealed that these areas are primarily concentrated in the eastern part of the study region, characterized by relatively steep slopes (Figure 13). These locations correspond to the rear edges of older landslides, exhibiting favorable conditions for failure but poor stability. Following the actual earthquake, only the eastern landslide area experienced a landslide event. This occurrence can be attributed to the controlling effects of the regional stress field direction, seismic wave propagation direction, and block movement direction, indicating that slope orientation is a significant topographical factor influencing the distribution of earthquake-induced landslides. According to Tian Yingying [41], the dominant slope orientations for landslides triggered by the 2013 Min County earthquake in Gansu Province were SE, S, and SW. In contrast, the slope orientation of the high landslide-prone area in the eastern region, which was not situated in a landslide source area, is E. Therefore, the absence of landslides in this area may be attributed to its slope orientation.

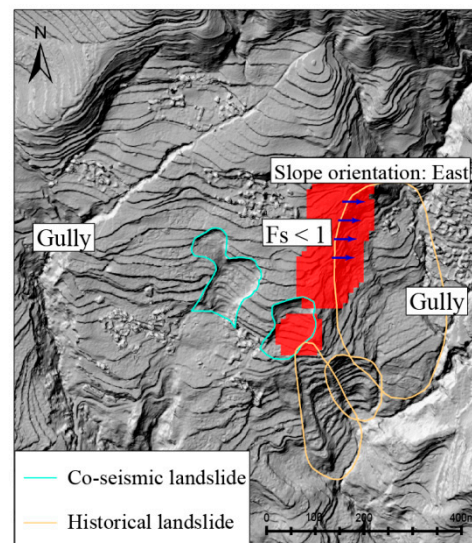


Figure 13. Historical landslide distribution in the study area.

5.3. Exploration of the Applicability of Predicting Groundwater Levels Using the 1 m Depth Temperature Method Combined with the RF Model

Common methods for groundwater investigation, such as seismic exploration, electrical resistivity surveys, and natural radioactivity methods, are physical indirect detection techniques [12]. However, these geophysical methods cannot provide specific details about the flow paths or scale of groundwater in vein-like distributions. In contrast, the 1 m depth ground temperature survey can effectively address these limitations. However, it still has certain drawbacks: first, the groundwater veins in the surveyed area must be shallow and sufficiently large; second, when conducting 1 m ground temperature surveys in larger study areas, the costs, workload, and time involved significantly increase. In the groundwater level prediction method proposed in this study, which combines the 1 m ground temperature method with a random forest model, the ground temperature distribution data serve as the key training variable for predicting the spatial distribution of groundwater levels. Thus, the method's applicability to other regions depends on whether those regions are suitable for 1 m ground temperature surveys. Other training variables can be selected based on regional characteristics, focusing on factors with significant impacts on groundwater, such as variations in soil permeability within the study area. Takeuchi [28] has noted that 1 m depth ground temperature surveys can be conducted when the ground temperature difference between the normal ground temperature at a depth of 1 m and the flowing groundwater temperature exceeds 2.5 °C.

In conclusion, the method combining the 1 m ground temperature method and random forest model is applicable to smaller study areas where the temperature difference between the normal ground temperature at a depth of 1 m and the flowing groundwater temperature exceeds 2.5 °C.

6. Conclusions

This study employed the 1 m depth ground temperature survey to investigate the shallow groundwater systems in the study area. Based on the results obtained from this method, a random forest model was utilized to perform regression predictions of the initial groundwater levels. Using precise hydrological and geotechnical parameters, the TRIGRS model was applied to assess the impact of actual rainfall on landslide stability. Furthermore, the Scoops3D model was integrated with the pore water pressures induced by actual rainfall and groundwater outputs from the TRIGRS model to analyze the stability of landslides in the study area under seismic conditions. The analysis focused on specific influencing factors contributing to the markedly different sliding characteristics observed in the two landslides triggered by the Min-Zhang earthquake. The results are as follows:

- (1) The combination of the 1 m depth ground temperature survey, high-density electrical resistivity method, and random forest model achieves an R^2 value of 0.93 for the initial prediction of groundwater levels in Yongguang Village, indicating that this approach can provide a relatively accurate estimate of the region's initial groundwater levels. This approach can be integrated with the TRIGRS model for predicting rainfall-induced landslide susceptibility in smaller areas.
- (2) The heavy rainfall occurring one day before the earthquake did not significantly decrease the stability of the Yongguang Village landslide. However, water infiltration increases the bulk density of the soil, softens the soil, and reduces its shear strength, thereby promoting slope deformation. The region's already abundant groundwater, combined with several months of preceding rainfall, contributed to elevated groundwater levels, creating conditions conducive to the occurrence of the westward landslide in Yongguang Village.
- (3) The primary triggering factor for both landslides in Yongguang Village is the earthquake; however, the eastward landslide is located at the back edge of an ancient landslide, characterized by a steeper slope and relatively less groundwater, resulting in instability induced by seismic inertial forces. In contrast, the westward landslide is situated in a relatively flat area that serves as a watershed with a low center and higher edges. The abundant groundwater there leads to a sharp increase in pore water pressure under seismic influence, reducing effective stress on the soil framework, ultimately resulting in liquefaction-triggered flow slides in loess.
- (4) The TRIGRS model combined with the Scoops3D model provides good predictive capabilities for rainfall-coupled landslides induced by earthquakes; however, it performs poorly for predicting flow slides triggered by liquefaction in loess, a specific type of geological hazard. For such unique landslides, greater emphasis should be placed on their distinctive hydrogeological conditions.

Author Contributions: Methodology, F.L. and K.L.; investigation, F.L., J.Z., and D.G.; writing—original draft, F.L.; writing—review and editing, S.X. and K.L.; funding acquisition, S.X. All authors have read and agreed to the published version of the manuscript.

Funding: This work was supported by the project of Central Public-interest Scientific Institution Basal Research Fund (2019IESLZ04, 2021IESLZ01); The Science for Earthquake Resilience of China Earthquake Administration (XH24043A); and 2024 Longyuan Young Talent Projects for Innovation and Entrepreneurship (2024QNTD51).

Data Availability Statement: Data available on request due to restrictions, e.g., privacy or ethical. The data presented in this study are available on request from the corresponding author. The data are not publicly available due to the requirements of the project.

Acknowledgments: We would like to express our gratitude to the research team involved in the field survey and to Liao Wang from Chengdu University of Technology for his invaluable guidance.

Conflicts of Interest: The authors declare no conflicts of interest.

References

1. Gao, G.; Hong, Y.; Geng, J.; Li, Y. Numerical simulation of saturated sand liquefaction discrimination and amplification effect. *J. Eng. Geol.* **2022**, *30*, 1874–1881.
2. Wang, L.; Chai, S.; Bo, J.; Wang, P.; Xu, S.; Li, X.; Pu, X. Triggering types, characteristics and disaster mechanism of seismic loess landslides. *Chin. J. Geotech. Eng.* **2023**, *45*, 1543–1554.
3. Zhang, X.; Pei, X.; Zhang, M.; Sun, P.; Jia, J. Experimental study on mechanism of flow slide of loess landslides triggered by strong earthquake: A case study in Dangjiachao, Ningxia province. *J. Eng. Geol.* **2018**, *26*, 1219–1226.
4. Lin, Q.; Cheng, Q.; Li, K.; Wang, Y.; Liu, S. Review on fragmentation-related dynamics of rock avalanches. *J. Eng. Geol.* **2023**, *31*, 815–829.
5. Wang, L.; Xu, S.; Wang, P.; Wang, R.; Che, A.; Zhou, Y.; Wu, Z.; Wang, Q.; Pu, X.; Chai, S.; et al. Characteristics and lessons of liquefaction-triggered large-scale flow slide in loess deposit during Jishishan M6.2 earthquake in 2023. *Chin. J. Geotech. Eng.* **2024**, *46*, 235–243.

6. Xu, Q.; Peng, D.; Fan, X.; Dong, X.; Zhang, X.; Wang, X. Preliminary study on the characteristics and initiation mechanism of Zhongchuan town flowslide triggered by Jishishan Ms 6.2 earthquake in Gansu Province. *Geomat. Inf. Sci. Wuhan Univ.* **2024**. [[CrossRef](#)]
7. Chen, L.; Wang, Y.; Yuan, X.; Li, Z.; Wang, Y.; Nie, G.; Zhang, H. Preliminary analysis for the triggering of soil flowslide that occurred in Zhongchuan Town following the 2023 Jishishan MS6.2 earthquake in Gansu Province. *J. Earthq. Eng. Eng. Vib.* **2024**, *44*, 187–193.
8. Xu, S.; Wu, Z.; Sun, J.; Yan, W.; Su, H.; Su, Y.J.C.E.E.J. Study of the characteristics and inducing mechanism of typical earthquake landslides of the Minxian-Zhangxian Ms6. 6 earthquake. *China Earthq. Eng. J.* **2013**, *35*, 471–476.
9. Zhi-jian, W.; Yu-jin, C.; Qian, W.; Duo-yin, Z.; Dan, Z. Disaster-causing mechanism of Yongguang landslide under Minxian-Zhangxian Ms6. 6 earthquake. *Chin. J. Geotech. Eng.* **2019**, *41* (Suppl. S2), 165–168.
10. Wang, Q.; Wang, Z.M.; Su, Y.Q.; Zhong, X.M.; Wang, L.M.; Ma, H.P.; Zhang, G.X.; Woolery, E.E.; Liu, K. Characteristics and mechanism of the landslide in Yongguang village, Minxian County, China. *Nat. Hazards* **2021**, *105*, 1413–1438. [[CrossRef](#)]
11. Zhang, J.; Chen, C.; Wu, C.; Zhang, Y. Development of An Image-based Borehole Flowmeter for Real-time Monitoring of Groundwater Flow Velocity and Direction in Landslide Boreholes. *IEEE Sens. J.* **2024**. *early access*. [[CrossRef](#)]
12. Chen, X. Study on Forward and Inverse Problems to Shallow Temperature Measurement for the Groundwater Flow Investigating. Ph.D. Thesis, Jilin University, Jilin, China, 2007.
13. Kappelmeyer, O. The use of near surface temperature measurements for discovering anomalies due to causes at depths. *Geophys. Prospect.* **1957**, *5*, 239–258. [[CrossRef](#)]
14. Furuya, G.; Suemine, A.; Sassa, K.; Komatsubara, T.; Watanabe, N.; Marui, H. Relationship between groundwater flow estimated by soil temperature and slope failures caused by heavy rainfall, Shikoku Island, southwestern Japan. *Eng. Geol.* **2006**, *85*, 332–346. [[CrossRef](#)]
15. Furuya, G.; Suemine, A.; Wang, G.H.; Takano, Y.; Ichikawa, Y. Vein of Groundwater Flow Behavior in a Land-Slide by Continuous Monitoring of Ground Temperature. In Proceedings of the 12th International IAEG Congress, Turin, Italy, 15–19 September 2014; Springer International Publishing AG: Cham, Switzerland, 2015; pp. 151–154.
16. Yasuda, T.; Takeuchi, A.; Kararia, T.N. Ground temperature measurement for mitigation of landslides: A case study in Japan and its application to Bhutan. *J. Nepal Geol. Soc.* **2016**, *50*, 73–81. [[CrossRef](#)]
17. Salciarini, D.; Godt, J.W.; Savage, W.Z.; Baum, R.L.; Conversini, P. Modeling landslide recurrence in Seattle, Washington, USA. *Eng. Geol.* **2008**, *102*, 227–237. [[CrossRef](#)]
18. Reid, M.E.; Christian, S.B.; Brien, D.L.; Henderson, S.T. *Scoops3D: Software to Analyze 3D Slope Stability Throughout a Digital Landscape*; 2328-7055; US Geological Survey: Reston, VA, USA, 2015.
19. Tran, T.V.; Alvioli, M.; Lee, G.; An, H.U. Three-dimensional, time-dependent modeling of rainfall-induced landslides over a digital landscape: A case study. *Landslides* **2018**, *15*, 1071–1084. [[CrossRef](#)]
20. Yang, L.; Cui, Y.L.; Xu, C.; Ma, S.Y. Application of coupling physics-based model TRIGRS with random forest in rainfall-induced landslide-susceptibility assessment. *Landslides* **2024**, *21*, 2179–2193. [[CrossRef](#)]
21. Gioia, E.; Speranza, G.; Ferretti, M.; Godt, J.W.; Baum, R.L.; Marincioni, F. Application of a process-based shallow landslide hazard model over a broad area in Central Italy. *Landslides* **2016**, *13*, 1197–1214. [[CrossRef](#)]
22. Marin, R.J.; García, E.F.; Aristizábal, E. Assessing the Effectiveness of TRIGRS for Predicting Unstable Areas in a Tropical Mountain Basin (Colombian Andes). *Geotech. Geol. Eng.* **2021**, *39*, 2329–2346. [[CrossRef](#)]
23. Wu, J.Q.; Dai, F.C.; Liu, P.; Huang, Z.Q.; Meng, L.C. Application of the electrical resistivity tomography in groundwater detection on loess plateau. *Sci. Rep.* **2023**, *13*, 14. [[CrossRef](#)]
24. Wu, W.; Wang, G.; Zhang, G.; Feng, L.; Yao, Z.; Su, X. Long-runout characteristics of the Yongguang 1# loess flowslide in Minxian County, Gansu Province. *Chin. J. Geol. Hazard Control* **2023**, *34*, 3–12.
25. Liu, K. Earthquake-Induced Failure Mechanism and Stability Evaluation of Loess Slope Under Rainfall Effects. PhD Thesis, Lanzhou University, Lanzhou, China, 2020.
26. Wang, L.; Pu, X.; Wu, Z.; Sun, J.; Wang, P.; Chai, S.; Xu, S.; Deng, J. The shaking table test of the instability sliding of loess slope under the coupling effects of earthquake and rainfall. *Chin. J. Rock Mech. Eng.* **2017**, *36* (Suppl. S2), 3873–3883.
27. Xin, Y.; Sun, Q.; Bao, H.; Nan, J.; Jia, H.; Li, P. Study of direct shear damage characteristics of loess-hipparion red clay interface. *J. Eng. Geol.* **2023**, 1–21. Available online: <https://chn.oversea.cnki.net/kcms/detail/detail.aspx?filename=GCDZ20231031005&dbcode=CAPJ&dbname=CAPJLAST&uniplatform=NZKPT> (accessed on 26 November 2024).
28. Takeuchi, A. Method of investigating groundwater-vein streams by measuring one-meter-depth temperature in landslide areas part 1. *Jpn. Assoc. Groundw. Hydrol.* **1980**, *22*, 73–101.
29. Breiman, L. Random forests. *Mach. Learn.* **2001**, *45*, 5–32. [[CrossRef](#)]
30. Catani, F.; Lagomarsino, D.; Segoni, S.; Tofani, V. Landslide susceptibility estimation by random forests technique: Sensitivity and scaling issues. *Nat. Hazards Earth Syst. Sci.* **2013**, *13*, 2815–2831. [[CrossRef](#)]
31. Iverson, R.M. Landslide triggering by rain infiltration. *Water Resour. Res.* **2000**, *36*, 1897–1910. [[CrossRef](#)]
32. Baum, R.L.; Savage, W.Z.; Godt, J.W. *TRIGRS: A Fortran Program for Transient Rainfall Infiltration and Grid-Based Regional Slope-Stability Analysis, Version 2.0*; US Geological Survey: Reston, VA, USA, 2008.
33. Godt, J.W.; Baum, R.L.; Savage, W.Z.; Salciarini, D.; Schulz, W.H.; Harp, E.I. Transient deterministic shallow landslide modeling: Requirements for susceptibility and hazard assessments in a GIS framework. *Eng. Geol.* **2008**, *102*, 214–226. [[CrossRef](#)]

34. Li, B.; Zhang, F. Three-dimensional stability evaluation of shallow loess landslides under rainfall and earthquake conditions. *Chin. J. Eng.* **2022**, *44*, 440–450.
35. Lu, D.; Hu, Y.; Peng, S.; Xie, J. Application of shallow earth temperature survey in investigating the relationships of spatial distribution between the typical weathering slope collapse and groundwater. *Ecol. Environ. Sci.* **2011**, *20*, 208–216.
36. Catani, F.; Segoni, S.; Falorni, G. An empirical geomorphology-based approach to the spatial prediction of soil thickness at catchment scale. *Water Resour. Res.* **2010**, *46*, 15. [[CrossRef](#)]
37. Ren, L. Forming Mechanism of the Mudflow-Landslides in Loess Triggered by the Earthquake. Master's Thesis, Xi'an University of Science and Technology, Xi'an, China, 2016.
38. Chen, J.C.; Wang, L.M.; Pu, X.W.; Li, F.X.; Li, T.L. Experimental study on the dynamic characteristics of low-angle loess slope under the influence of long- and short-term effects of rainfall before earthquake. *Eng. Geol.* **2020**, *273*, 15. [[CrossRef](#)]
39. Li, L. Numerical Simulation Analysis on Site Effects in the Meizoseismal Area of the Minxian-Zhangxian Ms6.6 Earthquake. Master's Thesis, Lanzhou Institute of Seismology CEA, Lanzhou, China, 2018.
40. Zhang, J.R.; Lin, C.Y.; Tang, H.M.; Wen, T.; Tannant, D.D.; Zhang, B.C. Input-parameter optimization using a SVR based ensemble model to predict landslide displacements in a reservoir area—A comparative study. *Appl. Soft. Comput.* **2024**, *150*, 18. [[CrossRef](#)]
41. Tian, Y. Spatial Distribution and Geometrical Characteristic of Landslides Related to the 2013 Minxian Earthquake of Gansu Province. Master's Thesis, China University of Geosciences (Beijing), Beijing, China, 2016.

Disclaimer/Publisher's Note: The statements, opinions and data contained in all publications are solely those of the individual author(s) and contributor(s) and not of MDPI and/or the editor(s). MDPI and/or the editor(s) disclaim responsibility for any injury to people or property resulting from any ideas, methods, instructions or products referred to in the content.